Article

FeNi LDH/V$_2$CT$_x$/NF as Self-Supported Bifunctional Electrocatalyst for Highly Effective Overall Water Splitting

Liming Yang [1], **Tao Yang** [1,*] , **Yafeng Chen** [1], **Yapeng Zheng** [1], **Enhui Wang** [1], **Zhentao Du** [2], **Kuo-Chih Chou** [1] **and Xinmei Hou** [1,*]

[1] Beijing Advanced Innovation Center for Materials Genome Engineering, Collaborative Innovation Center of Steel Technology, University of Science and Technology Beijing, Beijing 100083, China; yangliming0619@163.com (L.Y.); yafeng_chen2013@163.com (Y.C.); zhengyapeng1994@163.com (Y.Z.); wangenhui@ustb.edu.cn (E.W.); kcc126@126.com (K.-C.C.)

[2] MOE Key Laboratory of New Processing Technology for Non-Ferrous Metals and Materials, Guangxi Key Laboratory of Processing for Non-Ferrous Metals and Featured Materials, Guangxi University, Nanning 530004, China; zhentaodu@126.com

[*] Correspondence: yangtaoustb@ustb.edu.cn (T.Y.); houxinmeiustb@ustb.edu.cn (X.H.)

Abstract: The development of bifunctional electrocatalysts with efficient oxygen evolution reaction (OER) and hydrogen evolution reaction (HER) is still a key challenge at the current stage. Herein, FeNi LDH/V$_2$CT$_x$/nickel foam (NF) self-supported bifunctional electrode was prepared via deposition of FeNi LDH on V$_2$CT$_x$/NF substrate by hydrothermal method. Strong interfacial interaction between V$_2$CT$_x$/NF and FeNi LDH effectively prevented the aggregation of FeNi LDH, thus exposing more catalytic active sites, which improved electrical conductivity of the nanohybrids and structural stability. The results indicated that the prepared FeNi LDH/V$_2$CT$_x$/NF required 222 mV and 151 mV overpotential for OER and HER in 1 M KOH to provide 10 mA cm^{-2}, respectively. Besides, the FeNi LDH/V$_2$CT$_x$/NF electrocatalysts were applied to overall water splitting, which achieved a current density of 10 mA cm^{-2} at 1.74 V. This work provides ideas for improving the electrocatalytic performance of electrocatalysts through simple synthesis strategies, structural adjustment, use of conductive substrates and formation of hierarchical structures.

Keywords: V$_2$CT$_x$ MXene; layered double hydroxide; nanohybrids; overall water splitting

1. Introduction

Electrocatalytic water splitting to produce H$_2$ and O$_2$ as a green and efficient energy carrier has gained wide recognition and attention in the past decades [1–4]. Electrocatalytic water splitting consists of the process of HER and OER at the cathode and anode, respectively. In both cases, it is greatly significant to explore efficient and low-cost electrocatalysts to reduce the excessive overpotential [5,6]. To date, the commonly used OER and HER electrocatalysts are the commercially IrO$_2$, RuO$_2$ materials and Pt/C materials [7,8]; however, the high cost, limited reserves and poor multifunctional properties greatly limit their applications in water splitting [9,10].

At present, non-noble M-based materials like layered double hydroxide (LDH) have received extensive attention because of their flexible structural composition, diversified synthesis techniques and excellent electrocatalytic activity are considered to be outstanding electrocatalysts for water splitting [11–17]. Among LDH materials, FeNi LDH has received much attention for its good physicochemical properties, excellent OER electrocatalytic properties and durability in alkaline media [18,19]. Although FeNi LDH has been proved to be efficient in electrocatalysis, there are still two obstacles to further enhancements [20–22]. The first obstacle is its low conductivity due to poor carrier mobilities [23]. Two ways can be taken to overcome this obstacle. One is to combine FeNi LDH with highly conductive materials, such as graphene [24], crystal carbon conjugated (g-C$_3$N$_4$) [25], two-dimensional

(2D) carbides and nitride (MXenes). The other is to grow FeNi LDH on a conductive skeleton, such as Al foil, Ni foam (NF), Ti sheet, carbon paper, carbon cloth and stainless steel mesh, etc [26,27]. The second obstacle is that aggregation of FeNi LDH leads to a reduction of its active site. There are some works that combined FeNi LDH and electric conducting graphene as a highly efficient electrocatalyst to enhance OER due to reducing aggregation [28,29]. Therefore, it is an effective method to introduce two-dimensional materials to enhance conductivity and increase restricted active sites of FeNi LDH.

As two-dimensional materials with a large specific surface area and high electrical conductivity [30], MXene has been extensively used in electrocatalyst applications in recent year [31–34]. In the MXene family, V_2CT_x has various oxidation states of vanadium ion, so that the V surface layer may produce pseudocapacitive behavior [35], thus promoting the charge transfer between adsorbent and V_2CT_x carrier. The previous work of our group has proved that the combination of V_2CT_x and FeNi LDH can enhance the conductivity of FeNi LDH, reduce agglomeration phenomenon, and has excellent ORR and OER, which can be applied to a zinc–air battery [36]. To further explore and enhance the electrocatalytic performance of FeNi LDH, FeNi LDH/ V_2CT_x was grown on NF to form a self-supporting electrode for efficient water splitting.

In this work, FeNi LDH/V_2CT_x/NF self-supporting electrode was obtained via one-step hydrothermal deposition of FeNi LDH nanosheets on V_2CT_x/NF substrate. Then, the properties of HER, OER and overall water splitting of FeNi LDH/V_2CT_x/NF were systematically studied. Lastly, the electrocatalytic mechanism of FeNi LDH/V_2CT_x/NF was explored by the density functional theory method.

2. Experimental Section

2.1. Materials

V_2AlC (99 wt%, 400 mesh) was purchased from Foshan Xinxi Technology Co., Ltd, Guangdong, China. Nickel foam (NF) was purchased from Taiyuan Power Source Technology Co., Ltd, China. HF (~40 wt%), $Fe(NO_3)_3 \cdot 9H_2O$ (96.8 wt%), $Ni(NO_3)_2 \cdot 6H_2O$ (98.0 wt%), N-Methylpyrrolidone (NMP), tetrapropylammonium hydroxide (TPAOH, 40 wt%) and urea (CH_4N_2O, 96.0 wt%) were purchased from Aladdin, Shanghai, China. RuO_2 (98.9 wt%), Pt/C (20 wt%) and Nafion solution (5 wt%) were purchased from Macklin, Shanghai, China.

2.2. Sample Preparation

2.2.1. Preparation of V_2CT_x

Firstly, 1.0g V_2AlC powder was gradually added to 20mL HF solution under stirring for 0.5 h and the suspension was kept stirring for 48 h at 55 °C. Secondly, the reaction mixture was rinsed with argon deoxygenated water and centrifuged. After that, the precipitate was re-dispersed to 20 mL TPAOH and stirred for 24 h. Next, the synthesized multilayer V_2CT_x was centrifuged and washed twice, freeze-dried and weighed for V_2CT_x MXene. V_2CT_x nanosheets suspension concentration is 8 mg mL^{-1}.

2.2.2. Preparation of V_2CT_x/NF

NFs ($1 \times 3 \times 0.1$ cm^3) were pretreated with concentrated HCl (3 M) for 0.5 h, and subsequently washed with acetone absolute ethanol and DI water. After that, NFs ($1 \times 3 \times 0.1$ cm^3) were placed in 20 mL MXene suspension for 1 h. MXene is firmly adsorbed on the surface of NF by electrostatic adsorption, and V_2CT_x/NF is prepared. After repeated washing with Ar de-aerated DI water, vacuum drying for later use.

2.2.3. Preparation of FeNi LDH/V_2CT_x/NF

FeNi LDH/V_2CT_x/NF was synthesized by the hydrothermal method. 100 mM urea, 5 mM $Fe(NO_3)_3 \cdot 9H_2O$ and 15 mM $Ni(NO_3)_2 \cdot 6H_2O$ were dissolved in 5 mL of DI water, stirring for 0.5 h to form a mixed solution (named solution A). 25 mL NMP was added to solution A and continued to stir for 0.5 h (named solution B). Then, V_2CT_x/NFs

($1 \times 3 \times 0.1$ cm^3) were placed in solution B and heated for 12 h at 120 °C. For comparison, FeNi LDH/NF, V$_2$CT$_x$/NF and Ni(OH)$_2$ V$_2$CT$_x$/NF was synthesized with the same process. The load of electrocatalyst was measured by weighing the NF electrode before and after electrocatalyst growth. In this report, for FeNi LDH/V$_2$CT$_x$/NF, the electrocatalyst load was about 5 mg cm^{-2}.

2.2.4. Preparation of RuO$_2$/NF and Pt/C/NF

The RuO$_2$ (10 mg) was dispersed ultrasonically in a mixture of isopropanol (750 μL), Nafion (16 μL, 5.0 wt%) and deionized water (250 μL). The suspension was ultrasonic for 30min to obtain an evenly dispersed ink solution. Then, 500 μL of electrocatalyst ink was loaded on 1×1 cm^2 NF and the electrocatalyst load is about 5 mg cm^{-2}. The process for preparing Pt/C/NF is the same, except that commercial Pt/C (20 wt%) is used instead of commercial RuO$_2$.

2.3. Materials Characterization

The morphology was studied by field emission scanning electron microscopy (FESEM, FEI Zeiss Sigma 300). Transmission electron microscopy (TEM) was recorded using an FEI TalosF200x. Powder XRD pattern was obtained by Cu-Kα (λ = 0.1540 nm) on a SMARTLAB (9) X-ray photoelectron spectroscopy (XPS); the signal was captured using Axis Ultra DLD Kratos AXIS SUPRA.

2.4. Electrochemical Measurements

The electrocatalytic property was determined using a standard three-electrode system in 1.0 M KOH solution on a CHI 760E electrochemical workstation. FeNi LDH/V$_2$CT$_x$/NF served as the working electrode, carbon rod (OER) or platinum plate (HER) and Hg/HgO electrode (1 M KOH solution) were served as the counter electrode and reference electrode, respectively. According to the Nernst Equation (E_{RHE} = $E_{Hg/HgO}$ + 0.059 pH + 0.098 V), all potentials measured at the Hg/HgO electrode in this study were converted to potentials with the reversible hydrogen electrode (RHE). OER and HER were measured under the condition of O$_2$ and Ar saturation, respectively. Until the electrochemical data were tested, the working electrode was electrochemically activated for cyclic voltammetry 50 times. All the linear sweep voltammetry (LSV) curves are tested at 5 mV s^{-1} with 100% iR-compensation. The linear part of the Tafel curve was fitted according to the Tafel equation, and the Tafel slope was obtained to estimate the kinetic performance of the prepared electrocatalyst. Electrochemical impedance spectroscopy (EIS) was measured in the frequency range of 10^{-2} to 10^6 Hz. The double layer capacitance (C_{dl}) of the electrocatalysts was obtained by cyclic voltammetry at different scanning rates at non-Faraday potentials, and the ECSA of the catalysts was calculated. At room temperature, the prepared electrodes acted directly for overall water splitting in a two-electrode cell.

2.5. DFT Calculation Details

Vienna AB-Initio Simulation Package using the projector augmented wave (PAW) method was applied for all DFT calculations [37,38]. The local d-electrons of Ni and Fe in hydroxides were described by the DFT+U method. The value of U-J was 3.3 eV for V, 6.4 eV for Ni and 4.3 eV for Fe [9,39–41]. In order to simulate FeNi LDH/MXene nanohybrid, Fe doped NiOOH monolayer adsorption on O end V$_2$CT$_x$ was considered to simulate the electrocatalyst [42]. Since it is difficult to measure the crystal orientation of Fe-doped NiOOH intermediates, a surface exposed (001) Fe-doped NiOOH layer was coupled with V$_2$CT$_x$ to obtain the model with the most favorable energy structure and the lowest lattice mismatch for subsequent calculation. A 2×2 supercell of FeNi LDH and V$_2$CT$_x$ monolayer was constructed to become an 11.69 Å $\times$ 11.69 Å cell with a 16 Å vacuum space. Every four Ni atoms are replaced by one Fe atom. The whole calculation process uses the K-point grid with dimensions of $3 \times 3 \times 1$. During the structure optimization, the tolerance of residual

force for each atom is 0.05 eV/Å. When two consecutive self-consistent calculations are performed, the energy difference does not exceed 10^{-4} eV.

3. Results and Discussion

3.1. Preparation and Characterization of FeNi LDH/V_2CT_x/NF

The synthesis scheme of FeNi LDH/V_2CT_x/NF is shown in Figure 1a. First, the Al layer of massive V_2AlC powder was removed by 40 wt% HF selective etching to prepare multilayer V_2CT_x. After TPAOH intercalation and ultrasonic dissection, V_2CT_x nanosheets with fewer layers and higher surface functional groups ($-F$, $-OH$) were obtained, which was beneficial to electrostatic adsorption on nickel foam and the nucleation and anchoring of FeNi LDH on V_2CT_x surface. Then, NF was immersed in V_2CT_x nanosheet suspension to obtain a V_2CT_x/NF electrode. After that, FeNi LDH nanosheets were hydrothermally deposited on V_2CT_x/NF substrate to obtain FeNi LDH/V_2CT_x/NF self-supported electrode. The XRD patterns of V_2AlC and few-layer V_2CT_x are illustrated in Figure 1b. The peaks of 41.3°and 13.5° correspond with the (103) and (002) crystal planes of V_2AlC, respectively (PDF#29−0101). The peaks at 41.3°and 13.5° disappear completely for the exfoliated few-layer V_2CT_x, and the characteristic peak (002) is reduced to 6.74°, indicating that the Al atoms of few-layer V_2CT_x are completely removed, and the C-lattice parameters increase [33,43,44]. In addition, the full and magnification XRD of the FeNi LDH/V_2CT_x/NF peeled off the nickel foam are shown in Figure S1 and Figure 1c. The peaks of $2\theta = 44.5°$, 51.9° and 76.37° correspond to the (111), (200), and (220) planes of Ni (PDF#04-0850). As shown in Figure 1c, the peaks at $2\theta = 7.28°$ coincided very well with (002) crystal planes of V_2CT_x, while the peaks at $2\theta = 11.41°$, 22.974°, 34.425°, and 61.254° were in good agreement with the (003), (006), (012) and (113) of the FeNi LDH (PDF#40-0215), respectively; these results showed that FeNi LDH/V_2CT_x/NF had been successfully prepared.

The pristine V_2AlC powders present bulk-like shapes (Figure S2) and unintercalated V_2CT_x exhibits an accordion-like morphology (Figure 1d and Figure S3). V_2CT_x nanosheets with a size of 200–300 nm and many edge defects were obtained by further intercalation and ultrasonic exfoliation of TPAOH (Figure 1e). As shown in Figure S4, the clear Tyndall effect in the supernatant illustrates the uniformly dispersed layers of V_2CT_x. Because of the electrostatic interaction between the positively charged NF substrate and the negatively charged V_2CT_x surface, V_2CT_x is able to anchor to the 3D NF structure, with silver NF turning into black NF (Figure S5). The low magnification SEM image of the FeNi LDH/V_2CT_x/NF sample can be seen in Figure 1g and the corresponding high magnification SEM image is shown in Figure 1h. The thickness of FeNi LDH nanosheets is about 8.03 nm (Figure S6). FeNi LDH is evenly distributed over the surface of the V_2CT_x/NF substrate. As a comparison, FeNi LDH was grown directly on NF without V_2CT_x attached. It can be seen that FeNi LDH are clustered together (Figure 1f). The elemental mapping displays the well-distributed Fe, Ni, C and V elements in the FeNi LDH/V_2CT_x/NF (Figure S7); moreover, the TEM image of peeling FeNi LDH/V_2CT_x from nickel foam (Figure 1i) indicates loose flake texture grows on the surface of V_2CT_x with fewer layers and Figure 1j shows the interplanar spacing of 0.23 nm and 0.25 nm corresponding to (015) of FeNi LDH and the (100) of V_2CT_x, respectively. There are multiple diffraction rings on the (110) and (100) planes of V_2CT_x and the (015) plane of FeNi LDH in the regional electron diffraction image selected in Figure 1j. The even distribution of V, Ni, Fe, O and C in the FeNi LDH/V_2CTx nanohybrid is observed in Figure 1k.
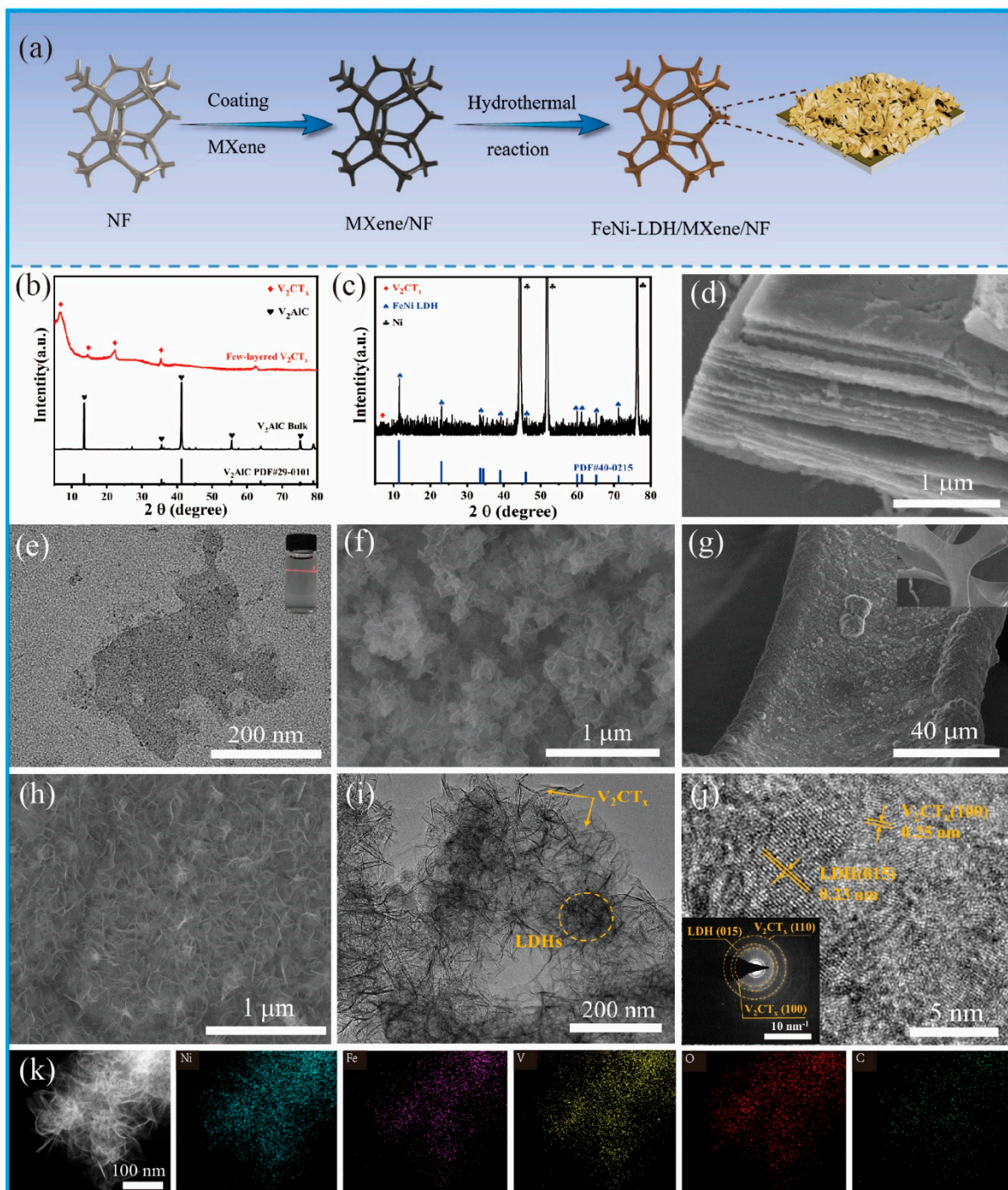
Figure 1. (**a**) Synthetic route of FeNi LDH/V_2CT_x/NF. SEM images of multilayered V_2CT_x (**b**) XRD of V_2AlC and V_2CT_x. (**c**) XRD patterns of FeNi LDH/V_2CT_x peeled off the nickel foam. (**d**) with TEM images of few-layer V_2CT_x (**e**), FeNi LDH/NF sample (**f**) and FeNi LDH/V_2CT_x/NF sample (**g**,**h**). TEM images of FeNi LDH/V_2CT_x nanohybrids peeled from NF (**i**), HRTEM images of FeNi LDH/V_2CT_x nanohybrids (**j**), the HAADF-STEM images in (**k**).

The XPS spectra of the FeNi LDH/V_2CT_x/NF sample showed Fe, Ni, V, O and C signal peaks (Figure 2a). Since V_2CT_x/NF is covered by NiFe LDH, the signal peak of V is very weak. The high-resolution O 1s XPS spectra (Figure S8) were deconvolution at about 532.98 eV, 531.78 eV and 530.84 eV to obtain three component peaks corresponding to H-O-H, M-OH and M-O, respectively. In the Ni 2p XPS spectrum (Figure 2b), the two characteristic peaks of $2p_{1/2}$ and $2p_{3/2}$ orbits of Ni^{2+} are located at 874.38 eV and

856.59 eV, respectively [45]. Similarly, in Fe 2p spectra (Figure 2c), peaks at 725.98 eV and 712.75 eV are due to $2p_{1/2}$ and $2p_{3/2}$ orbits of Fe^{3+}, respectively [46]. In contrast, for FeNi LDH/V_2CT_x/NF samples, the positive displacement of the Ni 2p peak is 0.6–0.65 eV and the Fe 2p peak is 0.43 eV. The higher the binding energy is, the higher the oxidation state of Fe and Ni iron after V_2CT_x binding is. Specifically, the electron transfer from V_2CT_x to LDHs increased the valence states of Fe and Ni, suggesting that there is a strong chemical interaction between FeNi LDH and V_2CT_x. Figure 2d shows the V 2p spectra, the V^{4+} of V_2CT_x corresponds to the V $2p_{1/2}$ at 524.25 and V $2p_{3/2}$ at 516.91 eV [47].
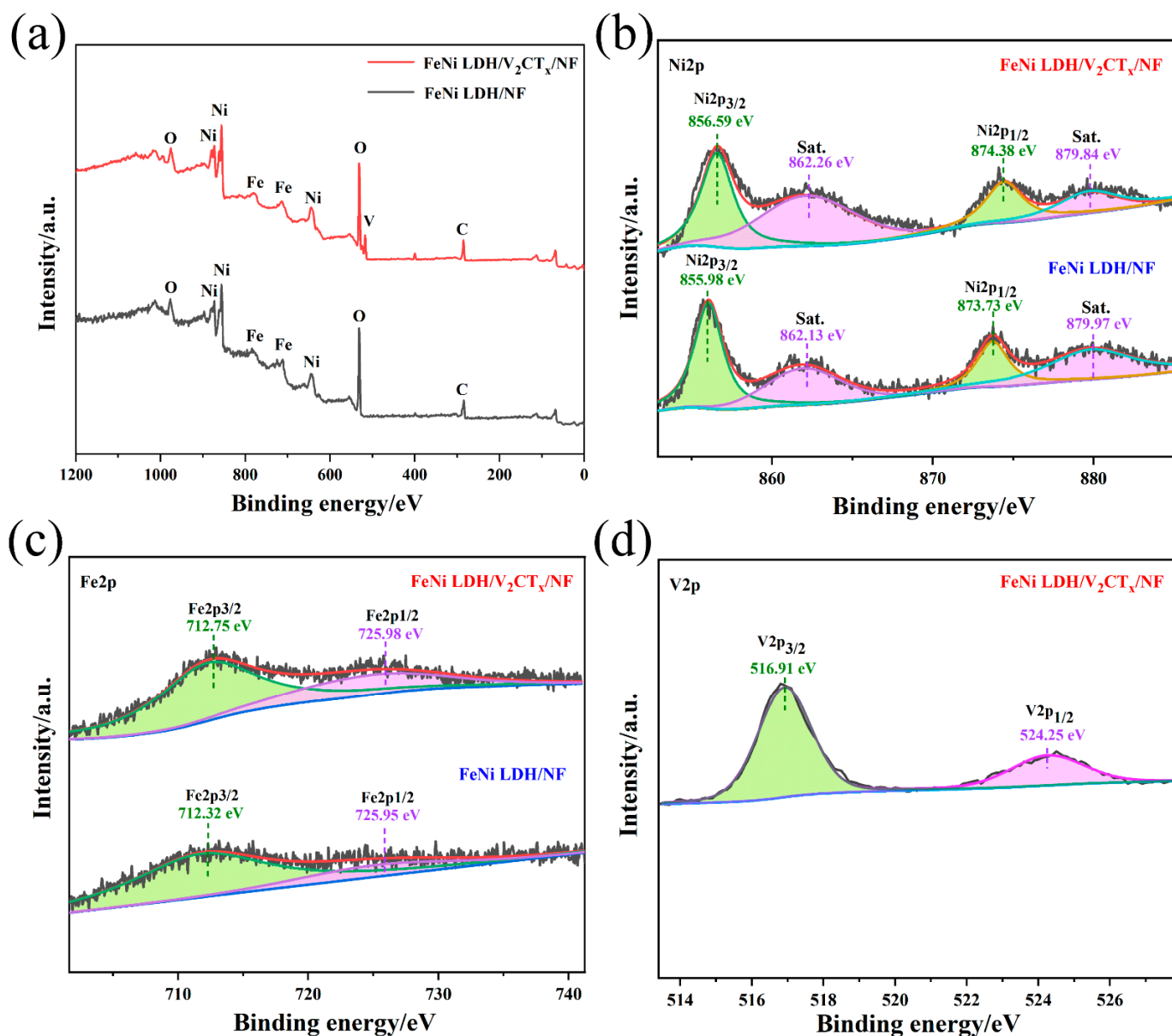

Figure 2. (**a**) Survey spectra of FeNi LDH/V_2CT_x/NF sample; (**b**,**c**) Ni 2p and Fe 2p XPS spectra of FeNi LDH/NF sample, respectively. (**d**) V 2p XPS spectra of FeNi LDH/V_2CT_x/NF.

3.2. Electrochemical Characterization

The OER electrocatalytic property of the prepared electrocatalyst was evaluated in 1.0 M KOH electrolyte with O_2-saturated. The activation process of FeNi LDH/V_2CT_x/NF electrocatalyst is shown in Figure S9. After 50 cycles of voltammetry, the electrocatalyst is transformed from hydroxide to oxyhydroxides. The redox peaks of the Ni(II)/Ni(III) are located at the potential range of 1.25–1.55 V (vs. RHE) [48], which was the strongest

at 1.39 V potential. As seen in Figure 3a, FeNi LDH/V_2CT_x/NF electrocatalyst with a minimum overpotential of 222 mV to achieve 10 mA cm^{-2} (η_{10} = 222 mV) exhibits highest catalytic activity, as compared with NF electrocatalysts (η_{10} = 400 mV), V_2CT_x/NF electrocatalysts (η_{10} = 380 mV), Ni(OH)$_2$/V_2CT_x/NF electrocatalysts (η_{10} = 326 mV) and RuO$_2$/NF (η_{10} = 265 mV); moreover, FeNi LDH/V_2CT_x/NF electrocatalyst achieves 50 mA cm^{-2} with the lowest overpotential of 265 mV (Figure 3b). Meanwhile, when comparing with the representative materials in Table S1 FeNi LDH/V_2CT_x/NF affords superior OER activity (η_{10} = 222 mV) to the excellent electrocatalysts reported recently, such as FeNi LDH/Ti$_3$C2T$_x$ (η_{10} = 298 mV) [15], CoNi-LDH/Ti$_3$C$_2$T$_x$ (η_{10} = 257 mV) [49], H$_2$PO^{2-}/FeNi LDH/V_2CT_x (η_{10} = 250 mV) [36] and N-CoFe LDH/NF (η_{10} = 233 mV) [50]. As seen in Figure 3c, the FeNi LDH/V_2CT_x/NF electrocatalyst shows the lowest Tafel slope of 58.7 mV dec^{-1}, as compared with FeNi LDH/NF (111.5 mV dec^{-1}), V_2CT_x/NF (786.9 mV dec^{-1}), Ni(OH)$_2$/V_2CT_x/NF (105.8 mV dec^{-1}), NF (1708.6 mV dec^{-1}) and commercial RuO$_2$/NF (67.9 mV dec^{-1}).
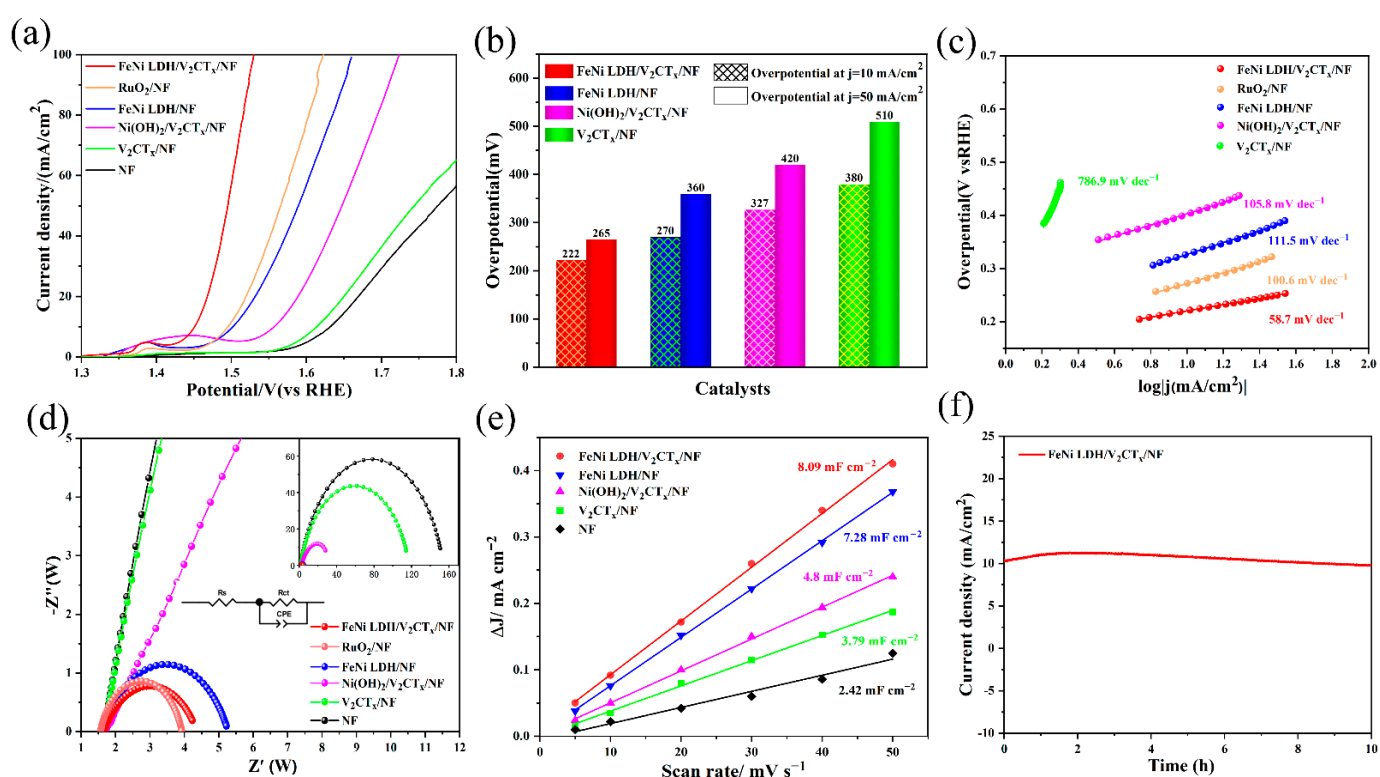

Figure 3. OER performances of prepared electrocatalysts. (**a**) LSV curves. (**b**) The overpotential of electrocatalysts. (**c**) Tafel plots. (**d**) EIS patterns. (**e**) C_{dl} of samples. (**f**) Stability measurements of FeNi LDH/V_2CT_x/NF.

Figure 3d shows the elliptic semicircle of the EIS diagram, in which the sharp reduction of the semicircle diameter in the high-frequency region demonstrates the acceleration of charge transfer. The FeNi LDH/V_2CT_x/NF electrocatalyst has the lowest charge transfer impedance (R_{ct} = 3.614 Ω) than that of Ni(OH)$_2$/V_2CT_x/NF (R_{ct} = 42.270 Ω) and FeNi LDH/NF (R_{ct} = 4.275 Ω) electrocatalyst according to Table S2. The electrochemically active surface areas (ECSAs) were estimated from the C_{dl} by cyclic voltammetry at 1.02–1.10 V (vs. RHE), as it is linear with ECSA (Figure S10). As shown in Figure 3e, the C_{dl} value of FeNi LDH/V_2CT_x/NF is 8.09 mF cm^{-2}, which is larger than those of FeNi LDH/NF (7.28 mF cm^{-2}), Ni(OH)$_2$/V_2CT_x/NF (4.8 mF cm^{-2}) and V_2CT_x/NF (3.79 mF cm^{-2}). Figure 3f shows the stability measurements of FeNi LDH/V_2CT_x/NF for η = 10 mA cm^{-2} at 0.222 V. The current density of FeNi LDH/V_2CT_x/NF did not decrease significantly after 10 h. After a 10h OER test, the morphology of FeNi LDH/V_2CT_x/NF

has not changed significantly (Figure S11), which further confirms its high stability. In addition, XPS measurements of FeNi LDH/V_2CT_x/NF were performed (Figure S12). From the high-resolution Ni 2p spectra and Fe 2p spectra (Figure S11a,b), it can be seen that the characteristic peaks of both Ni 2p and Fe 2p have a slight rise. The former indicates that Ni^{2+} is oxidized to Ni^{3+}, and the latter indicates that Fe is also partially oxidized, which is beneficial to accelerate the redox activity in the OER process; moreover, the two peaks of the V 2p spectrum (Figure S11c) are still located at 516.91 eV (V $2p_{3/2}$) and 524.25 eV (V $2p_{1/2}$), corresponding to the V^{4+} state, indicating its good stability during the OER.

To further explore the HER activity, FeNi LDH/V_2CT_x/NF with 1×1 cm^2 was served as the working electrode, while Pt plate, Hg/HgO (1 M KOH) and 1 M KOH were used as the counter electrode, reference electrode and electrolyte, respectively. The overpotential of FeNi LDH/V_2CT_x/NF at a current density of 10 mA cm^{-2} is 151 mV (η_{10} = 151 mV), which is smaller than that of FeNi LDH/NF (η_{10} = 198 mV), Ni(OH)$_2$ LDH/V_2CT_x/NF (η_{10} = 214 mV), V_2CT_x/NF (η_{10} = 252 mV) and NF (η_{10} = 305 mV), except for Pt/C/NF (η_{10} = 81 mV) (Figure 4a). As seen from Figure 4b, FeNi LDH/V_2CT_x/NF electrocatalyst achieves a current density of 50 mA cm^{-2} with the lowest overpotential of 274 mV; moreover, the Tafel slope of the FeNi LDH/V_2CT_x/NF was 136 mV/dec, which was lower than that of FeNi LDH/NF (148 mV dec^{-1}), Ni(OH)$_2$ LDH/V_2CT_x/NF (152 mV dec^{-1}) and V_2CT_x/NF (173 mV dec^{-1}) (Figure 4c), further confirmed the internal reaction kinetics of the prepared FeNi LDH/V_2CT_x/NF significantly accelerated.
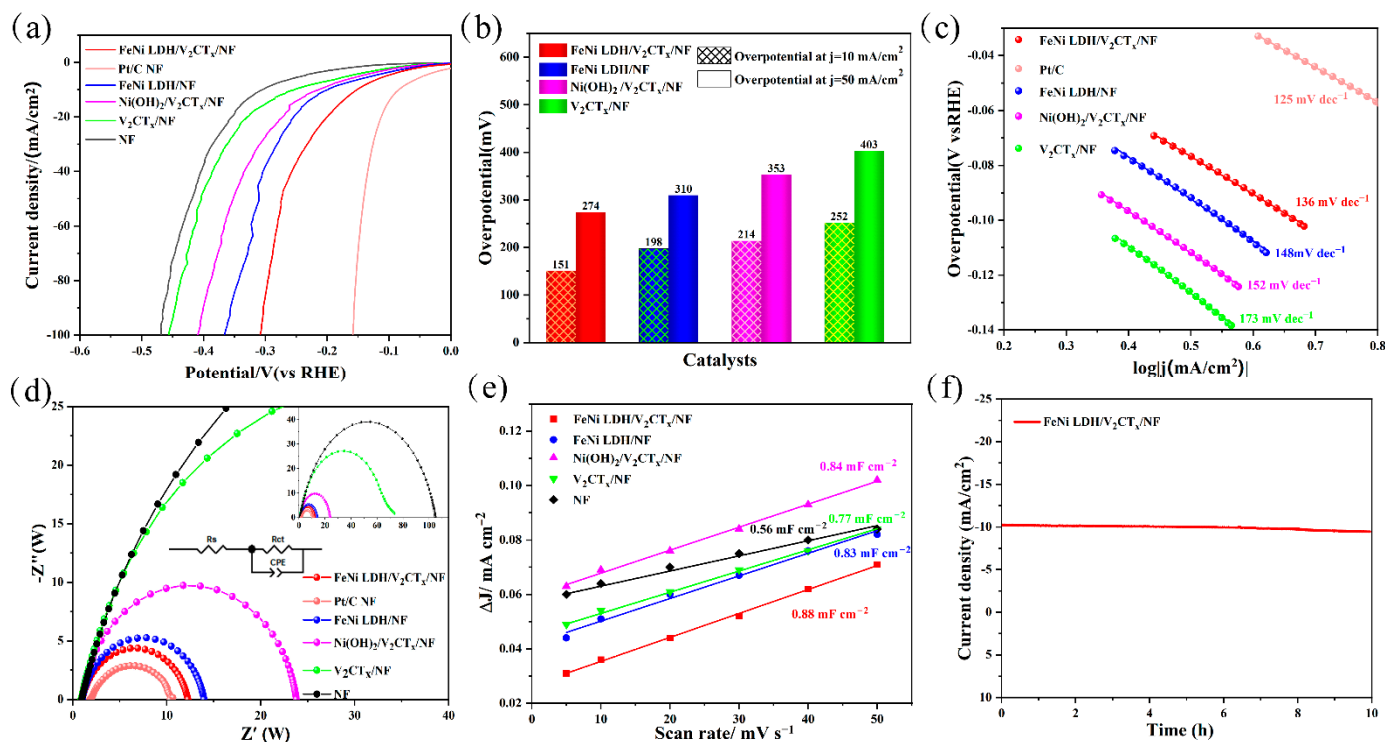

Figure 4. HER performances of prepared electrocatalysts. (**a**) LSV curves. (**b**) The overpotential of electrocatalysts. (**c**) Tafel plots. (**d**) EIS patterns. (**e**) C_{dl} of samples. (**f**) Stability measurements of FeNi LDH/V_2CT_x/NF.

EIS was tested at −1.0 V (vs. RHE). The results (Figure 4d and Table S3) showed that FeNi LDH/V_2CT_x/NF had the lowest R_{ct} (R_{ct} = 10.85 Ω) of all electrocatalysts, indicating good reaction kinetics and faster charge transfer. The CV curves were obtained between 0.123 to 0.223 V (vs RHE) to estimate the ECSA of all electrocatalysts (Figure S13). FeNi LDH/V_2CT_x/NF measured much higher C_{dl} (0.88 mF cm^{-2}) than FeNi LDH/NF (0.83 mF cm^{-2}), Ni(OH)$_2$ LDH/V_2CT_x/NF (0.84 mF cm^{-2}), V_2CT_x/NF (0.77 mF cm^{-2}) and NF (0.56 mF cm^{-2}) (Figure 4e). As shown in Figure 4f, the FeNi LDH/V_2CT_x/NF

electrocatalyst maintained excellent catalytic performance and showed better durability in alkaline solution after a 10 h cycling test at -10 mA cm^{-2}. As seen in Figure S14, the morphology of the electrocatalyst was well maintained after HER testing, indicating its good mechanical stability. Besides, Figure S15 shows the XPS spectra of Ni 2p, Fe 2p and V 2p in the FeNi LDH/V$_2$CT$_x$/NF before and after the durability test. No significant changes were observed, indicating high electrochemical stability.

Based on the results, the FeNi LDH/V$_2$CT$_x$/NF electrode can be used as a robust and efficient electrocatalyst for OER and HER. Therefore, the FeNi LDH/V$_2$CT$_x$/NF electrode was used as both cathode and anode in 1.0 M KOH for overall water splitting. It can be seen from Figure 5a that when the current density is 50 mA cm^{-2}, it is easy to achieve a voltage of 1.74 V (η_{50} = 1.74V), which is small than FeNi LDH/NF (η_{50} = 1.81 V), Ni(OH)$_2$ LDH/V$_2$CT$_x$/NF (η_{50} = 1.87 V) and V$_2$CT$_x$/NF (η_{50} = 1.92 V) (Figure 5b); moreover, FeNi LDH/V$_2$CT$_x$/NF has a superiority compared with other electrocatalysts prepared by the one-step hydrothermal method in the literature (Table S4), such as NiFe LDH/NiCoP/NF (1.75 V) [14], NiCo$_2$S$_4$@NiFe-LDH/NF (1.83 V) [51] and NiCo-LDH/NF (1.86 V) [52]. As can be seen from the LSV curve before and after 24 h of the overall water splitting test (Figure 5c), the performance of the electrocatalyst is relatively stable and the overpotential changes little at 10 mA cm^{-2}. Besides, the overall water splitting can be continued for 24 h steadily at 50 mA cm^{-2} (Figure 5d) and the O$_2$ and H$_2$ bubbles can be clearly observed (the inset of Figure 5d).

3.3. Mechanism Analysis

To further understand the interaction of FeNi LDH and V$_2$CT$_x$, the first-principles calculation was performed based on the DFT method (Figure 6). The side and top view of model structure of FeNi LDH/V$_2$CT$_x$ composite after structural relaxation are shown in Figure 6a and Figure S16. Figure 6b shows differential charge density in FeNi LDH/V$_2$CT$_x$ composite study the charge redistribution by subtracting the charge densities of FeNi LDH and V$_2$CT$_x$ slabs from the total charge density of the structure, which the light blue and yellow colors mean electron loss and electron gain, respectively. After V$_2$CT$_x$ is introduced, because V$_2$CT$_x$ has stronger electronegativity than FeNi LDH, electrons are transferred from FeNi LDH to V$_2$CT$_x$. The bader quantitative analysis shows that the amount of electron transfer from FeNi LDH to V$_2$CT$_x$ is 0.44 e$^-$ per unit cell, which may be due to the high electronegativity of V$_2$CT$_x$, which is easy to attract electrons from transition metal.

The project density of states (PDOS) and density of states (DOS) of FeNi LDH and FeNi LDH/V$_2$CT$_x$ are shown in Figure 6c,d. As exhibited in Figure 6c, compared with FeNi LDH, the electron density of FeNi LDH/V$_2$CT$_x$ near the Fermi level performs increased DOS and charge transfer, which is conducive to the adsorption–desorption performance of the reaction intermediates. Therefore, the conductivity of the electrocatalyst is improved and the energy barrier of OER is reduced [53,54]. As can be seen from Figure 6d, the PDOS of FeNi LDH/V$_2$CT$_x$ is further away from the Fermi energy level than that of FeNi LDH, where the D-band centers of FeNi LDH/V$_2$CT$_x$ and FeNi LDH are -2.96 eV and -2.77 eV, respectively. DFT simulations combined with experiments show that the increased activity is due to a modest downshift in the E_d level, which regulates the desorption and adsorption capacities of the intermediates according to D-band center theory [55,56]. Therefore, the balance between intrinsic activity adsorption capacity of electrocatalyst to intermediate should be considered. As illustrated in Figure 6e, FeNi LDH/V$_2$CT$_x$ shows an excellent electrocatalytic performance because of the increase of active sites and electrical conductivity.
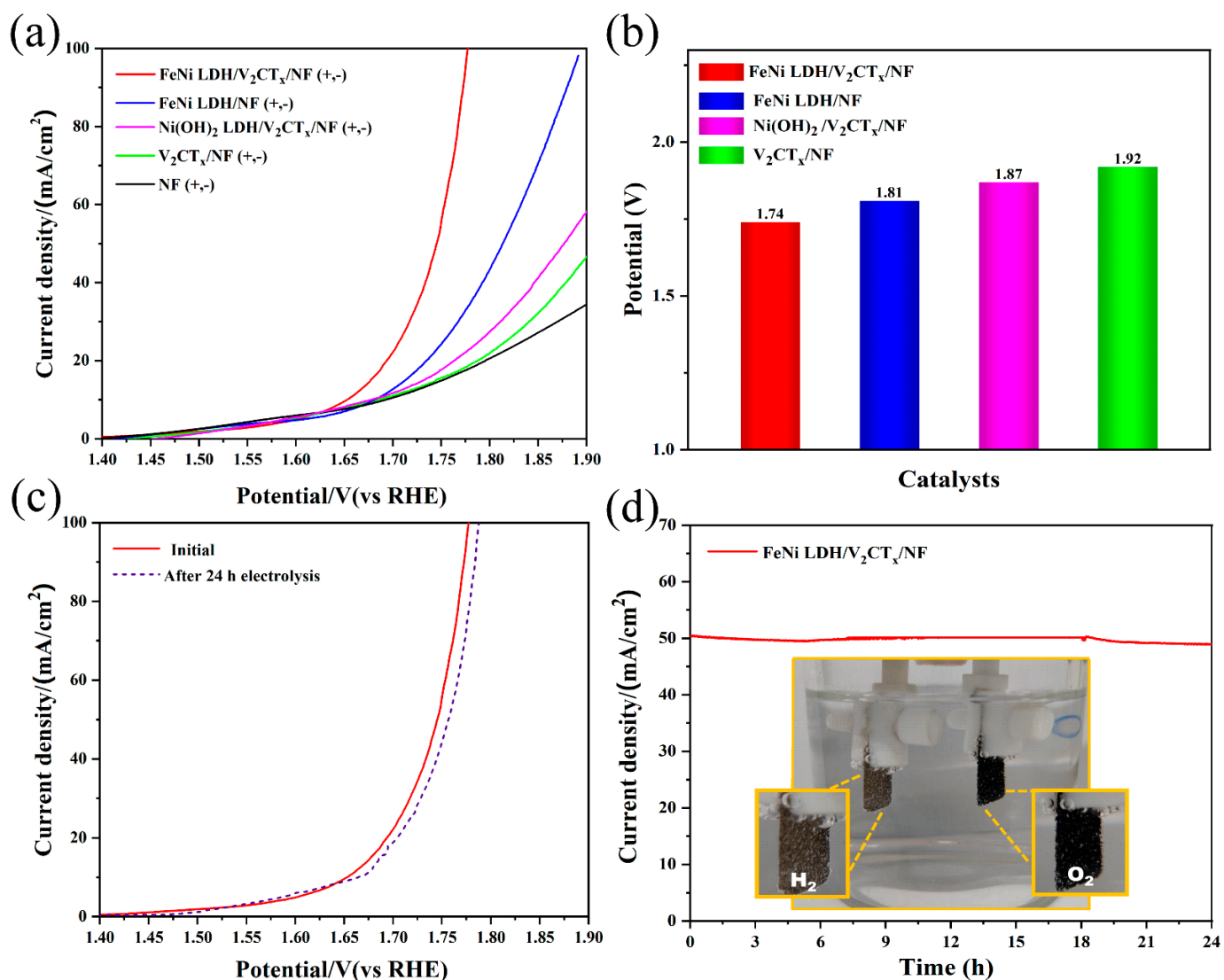
Figure 5. Overall water splitting performances of synthesized electrocatalysts. (**a**) LSV curves. (**b**) The voltage of electrocatalysts for overall water splitting. (**c**) LSV curves of FeNi LDH/V_2CT_x/NF before and after 15 h of electrolysis. (**d**) Stability measurements of FeNi LDH/V_2CT_x/NF. The inserted image shows the simultaneous production of H_2 and O_2 bubbles.

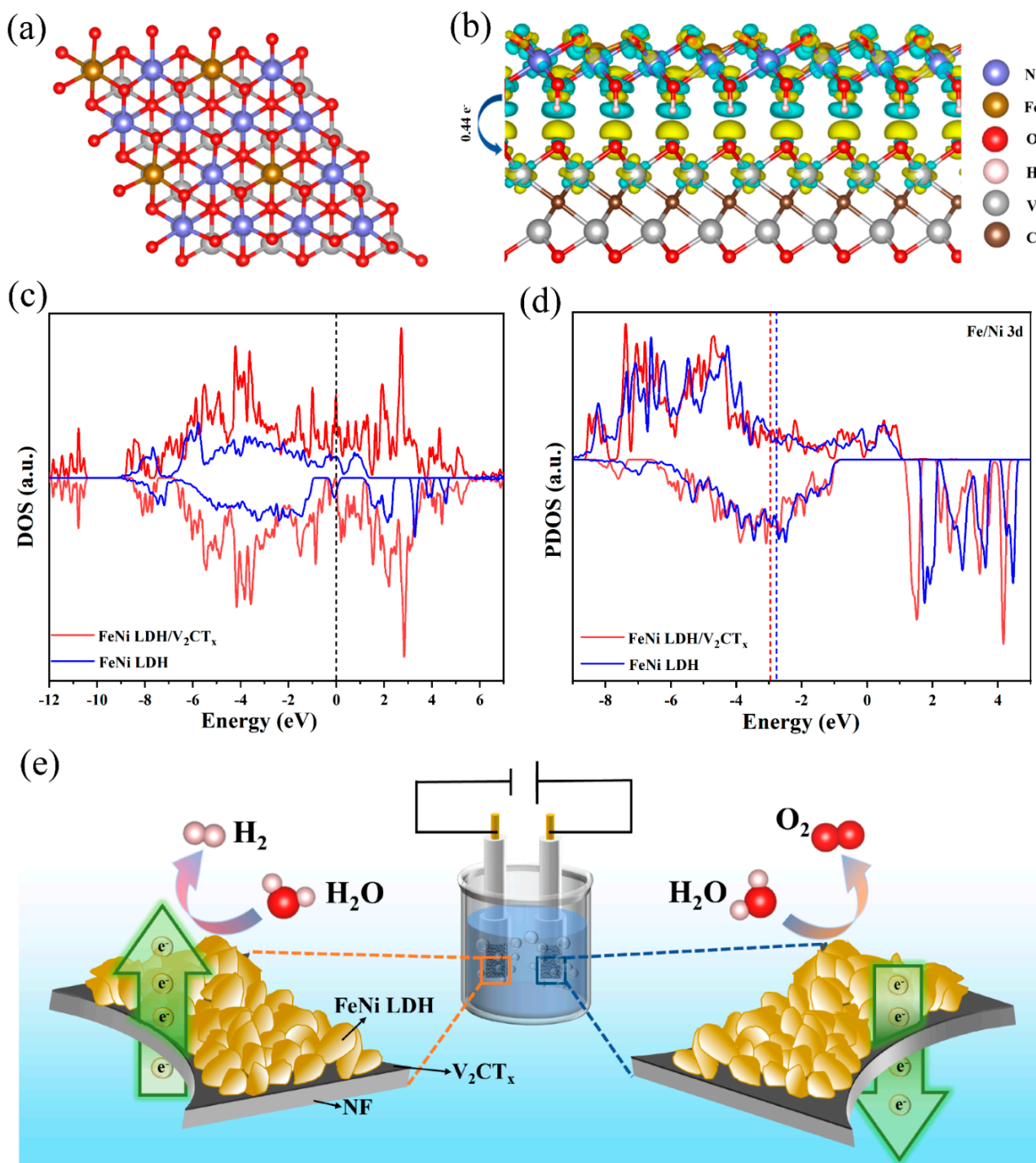**Figure 6.** (**a**) Top view of FeNi LDH/V_2CT_x composite. (**b**) Differential charge density in FeNi LDH/V_2CT_x composite. (**c**) DOS of FeNi LDH/V_2CT_x and FeNi LDH. The Fermi level is shifted to zero. (**d**) PDOS of FeNi LDH/V_2CT_x and FeNi LDH. (**e**) Illustration of the FeNi LDH/V_2CT_x/NF for OER and HER.

4. Conclusions

In summary, through a simple one-step hydrothermal method, a self-supported bifunctional FeNi LDH/V_2CT_x/NF electrode has been successfully prepared. The presence of V_2CT_x promoted the dispersed growth of FeNi LDH nanosheets onto V_2CT_x/NF working electrode and reduced the obstacle of electron transfer. The NF scaffold provides a highly exposed active surface and facilitates the electrolyte infiltration and gas dissipation

during OER. As a result, the overpotential of 222 mV and 151 mV of FeNi LDH/V_2CT_x/NF electrode at 10 mA cm^{-2} for the OER and the HER, respectively, proved an excellent electrocatalytic property. Besides, FeNi LDH/V_2CT_x/NF has a superiority (1.74 V) for overall water splitting at 50 mA cm^{-2} compared with other electrocatalysts prepared by one-step hydrothermal method in the literature; moreover, the current density of OER, HER and overall water splitting could remain almost the same after 10, 10 and 24 h test, underscoring the fundamentally improved of our bifunctional electrocatalysts.

Supplementary Materials: The following supporting information can be downloaded at: https://www.mdpi.com/article/10.3390/nano12152640/s1 [57–76].

Author Contributions: Conceptualization, L.Y. and T.Y.; methodology, L.Y.; software, Y.Z.; validation, L.Y., Y.C. and Z.D.; formal analysis, L.Y.; investigation, E.W. and L.Y.; resources, X.H. and K.-C.C.; data curation, L.Y.; writing—original draft preparation, L.Y.; writing—review and editing, L.Y. and T.Y.; visualization, Y.Z.; supervision, X.H.; project administration, T.Y.; funding acquisition, T.Y. All authors have read and agreed to the published version of the manuscript.

Institutional Review Board Statement: Not applicable.

Informed Consent Statement: Not applicable.

Data Availability Statement: Not applicable.

Conflicts of Interest: The authors declare no conflict of interest.

References

1. Du, P.; Eisenberg, R. Catalysts made of earth-abundant elements (Co, Ni, Fe) for water splitting: Recent progress and future challenges. *Energy Environ. Sci.* **2012**, *5*, 6012–6021. [CrossRef]
2. Yu, X.; Yu, Z.-Y.; Zhang, X.-L.; Li, P.; Sun, B.; Gao, X.; Yan, K.; Liu, H.; Duan, Y.; Gao, M.-R.; et al. Highly disordered cobalt oxide nanostructure induced by sulfur incorporation for efficient overall water splitting. *Nano Energy* **2020**, *71*, 104652. [CrossRef]
3. Bloor, L.G.; Molina, P.I.; Symes, M.D.; Cronin, L. Low pH Electrolytic Water Splitting Using Earth-Abundant Metastable Catalysts That Self-Assemble in Situ. *J. Am. Chem. Soc.* **2014**, *136*, 3304–3311. [CrossRef]
4. Wu, A.; Xie, Y.; Ma, H.; Tian, C.; Gu, Y.; Yan, H.; Zhang, X.; Yang, G.; Fu, H. Integrating the active OER and HER components as the heterostructures for the efficient overall water splitting. *Nano Energy* **2017**, *44*, 353–363. [CrossRef]
5. Wei, C.; Liu, C.; Gao, L.; Sun, Y.; Liu, Q.; Zhang, X.; Guo, J. MoS_2 nanosheets decorated $Ni(OH)_2$ nanorod array for active overall water splitting. *J. Alloys Compd.* **2019**, *796*, 86–92. [CrossRef]
6. Wan, L.; Wang, P. Recent progress on self-supported two-dimensional transition metal hydroxides nanosheets for electrochemical energy storage and conversion. *Int. J. Hydrogen Energy* **2020**, *46*, 8356–8376. [CrossRef]
7. Wang, T.; Wu, H.; Feng, C.; Zhang, L.; Zhang, J. MoP@NiCo-LDH on nickel foam as bifunctional electrocatalyst for high efficiency water and urea–water electrolysis. *J. Mater. Chem. A* **2020**, *8*, 18106–18116. [CrossRef]
8. Cao, Q.; Zhang, J.; Zhang, H.; Xu, J.; Che, R. Dual-surfactant templated hydrothermal synthesis of $CoSe_2$ hierarchical microclews for dielectric microwave absorption. *J. Adv. Ceram.* **2022**, *11*, 504–514. [CrossRef]
9. Lee, J.; Jung, H.; Park, Y.S.; Kwon, N.; Woo, S.; Selvam, N.C.S.; Han, G.S.; Jung, H.S.; Yoo, P.J.; Choi, S.M.; et al. Chemical transformation approach for high-performance ternary NiFeCo metal compound-based water splitting electrodes. *Appl. Catal. B Environ.* **2021**, *294*, 120246. [CrossRef]
10. Wang, B.; Cui, X.; Huang, J.-Q.; Cao, R.; Zhang, Q. Recent advances in energy chemistry of precious-metal-free catalysts for oxygen electrocatalysis. *Chin. Chem. Lett.* **2018**, *29*, 1757–1767. [CrossRef]
11. Sun, H.; Zhang, W.; Li, J.-G.; Li, Z.; Ao, X.; Xue, K.-H.; Ostrikov, K.K.; Tang, J.; Wang, C. Rh-engineered ultrathin NiFe-LDH nanosheets enable highly-efficient overall water splitting and urea electrolysis. *Appl. Catal. B Environ.* **2020**, *284*, 119740. [CrossRef]
12. Tian, M.; Jiang, Y.; Tong, H.; Xu, Y.; Xia, L. MXene-Supported FeCo-LDHs as Highly Efficient Catalysts for Enhanced Electrocatalytic Oxygen Evolution Reaction. *ChemNanoMat* **2019**, *6*, 154–159. [CrossRef]

13. Yang, Y.; Dang, L.; Shearer, M.J.; Sheng, H.; Li, W.; Chen, J.; Xiao, P.; Zhang, Y.; Hamers, R.J.; Jin, S. Highly Active Trimetallic NiFeCr Layered Double Hydroxide Electrocatalysts for Oxygen Evolution Reaction. *Adv. Energy Mater.* **2018**, *8*, 1703189. [CrossRef]

14. Zhang, H.; Li, X.; Hähnel, A.; Naumann, V.; Lin, C.; Azimi, S.; Schweizer, S.L.; Maijenburg, A.W.; Wehrspohn, R.B. Bifunctional Heterostructure Assembly of NiFe LDH Nanosheets on NiCoP Nanowires for Highly Efficient and Stable Overall Water Splitting. *Adv. Funct. Mater.* **2018**, *28*, 1706847. [CrossRef]

15. Yu, M.; Zhou, S.; Wang, Z.; Zhao, J.; Qiu, J. Boosting electrocatalytic oxygen evolution by synergistically coupling layered double hydroxide with MXene. *Nano Energy* **2018**, *44*, 181–190. [CrossRef]

16. Han, X.; Lin, Z.; He, X.; Cui, L.; Lu, D. The construction of defective FeCo-LDHs by in-situ polyaniline curved strategy as a desirable bifunctional electrocatalyst for OER and HER. *Int. J. Hydrogen Energy* **2020**, *45*, 26989–26999. [CrossRef]

17. Kim, S. Production of electrolyzed water for home-use based on electrodeposited macroporous platinum. *J. Mech. Sci. Technol.* **2017**, *31*, 1843–1849. [CrossRef]

18. Wan, L.; Zhao, Z.; Chen, X.; Liu, P.-F.; Wang, P.; Xu, Z.; Lin, Y.; Wang, B. Controlled Synthesis of Bifunctional NiCo$_2$O$_4$@FeNi LDH Core–Shell Nanoarray Air Electrodes for Rechargeable Zinc–Air Batteries. *ACS Sustain. Chem. Eng.* **2020**, *8*, 11079–11087. [CrossRef]

19. He, K.; Tadesse Tsega, T.; Liu, X.; Zai, J.; Li, X.H.; Liu, X.; Li, W.; Ali, N.; Qian, X. Utilizing the Space-Charge Region of the FeNi-LDH/CoP p-n Junction to Promote Performance in Oxygen Evolution Electrocatalysis. *Angew. Chem. Int. Ed. Engl.* **2019**, *58*, 11903–11909. [CrossRef]

20. Jeon, N.J.; Noh, J.H.; Yang, W.S.; Kim, Y.C.; Ryu, S.; Seo, J.; Seok, S.I. Compositional engineering of perovskite materials for high-performance solar cells. *Nature* **2015**, *517*, 476–480. [CrossRef]

21. Lai, M.; Kong, Q.; Bischak, C.; Yu, Y.; Dou, L.; Eaton, S.W.; Ginsberg, N.S.; Yang, P. Structural, optical, and electrical properties of phase-controlled cesium lead iodide nanowires. *Nano Res.* **2017**, *10*, 1107–1114. [CrossRef]

22. Conings, B.; Drijkoningen, J.; Gauquelin, N.; Babayigit, A.; D'Haen, J.; D'Olieslaeger, L.; Ethirajan, A.; Verbeeck, J.; Manca, J.; Mosconi, E.; et al. Intrinsic Thermal Instability of Methylammonium Lead Trihalide Perovskite. *Adv. Energy Mater.* **2015**, *5*, 1500477. [CrossRef]

23. Li, Z.; Wang, X.; Ren, J.; Wang, H. NiFe LDH/Ti3C2Tx/nickel foam as a binder-free electrode with enhanced oxygen evolution reaction performance. *Int. J. Hydrogen Energy* **2022**, *47*, 3886–3892. [CrossRef]

24. Jiao, Y.; Zheng, Y.; Davey, K.; Qiao, S.Z. Activity origin and catalyst design principles for electrocatalytic hydrogen evolution on heteroatom-doped graphene. *Nat. Energy* **2016**, *1*, 16130. [CrossRef]

25. Niu, W.; Marcus, K.; Zhou, L.; Li, Z.; Shi, L.; Liang, K.; Yang, Y. Enhancing Electron Transfer and Electrocatalytic Activity on Crystalline Carbon-Conjugated g-C$_3$N$_4$. *ACS Catal.* **2018**, *8*, 1926–1931. [CrossRef]

26. Bodhankar, P.M.; Sarawade, P.B.; Singh, G.; Vinu, A.; Dhawale, D.S. Recent advances in highly active nanostructured NiFe LDH catalyst for electrochemical water splitting. *J. Mater. Chem. A* **2020**, *9*, 3180–3208. [CrossRef]

27. Karmakar, A.; Karthick, K.; Sankar, S.S.; Kumaravel, S.; Madhu, R.; Kundu, S. A vast exploration of improvising synthetic strategies for enhancing the OER kinetics of LDH structures: A review. *J. Mater. Chem. A* **2020**, *9*, 1314–1352. [CrossRef]

28. Long, X.; Li, J.; Xiao, S.; Yan, K.; Wang, Z.; Chen, H.; Yang, S. A Strongly Coupled Graphene and FeNi Double Hydroxide Hybrid as an Excellent Electrocatalyst for the Oxygen Evolution Reaction. *Angew. Chem. Int. Ed.* **2014**, *53*, 7584–7588. [CrossRef] [PubMed]

29. Nayak, S.; Parida, K. Superactive NiFe-LDH/graphene nanocomposites as competent catalysts for water splitting reactions. *Inorg. Chem. Front.* **2020**, *7*, 3805–3836. [CrossRef]

30. Tang, H.; Hu, Q.; Zheng, M.; Chi, Y.; Qin, X.; Pang, H.; Xu, Q. MXene–2D layered electrode materials for energy storage. *Prog. Nat. Sci.* **2018**, *28*, 133–147. [CrossRef]

31. Guo, J.; Zhao, Y.; Liu, A.; Ma, T. Electrostatic self-assembly of 2D delaminated MXene (Ti$_3$C$_2$) onto Ni foam with superior electrochemical performance for supercapacitor. *Electrochim. Acta* **2019**, *305*, 164–174. [CrossRef]

32. Jiang, J.; Bai, S.; Yang, M.; Zou, J.; Li, N.; Peng, J.; Wang, H.; Xiang, K.; Liu, S.; Zhai, T. Strategic design and fabrication of MXenes-Ti3CNCl2@CoS2 core-shell nanostructure for high-efficiency hydrogen evolution. *Nano Res.* **2022**, *15*, 5977–5986. [CrossRef]

33. Lin, H.; Chen, L.; Lu, X.; Yao, H.; Chen, Y.; Shi, J. Two-dimensional titanium carbide MXenes as efficient non-noble metal electrocatalysts for oxygen reduction reaction. *Sci. China Mater.* **2018**, *62*, 662–670. [CrossRef]

34. Liu, F.; Zhou, J.; Wang, S.; Wang, B.; Shen, C.; Wang, L.; Hu, Q.; Huang, Q.; Zhou, A. Preparation of High-Purity V$_2$C MXene and Electrochemical Properties as Li-Ion Batteries. *J. Electrochem. Soc.* **2017**, *164*, A709–A713. [CrossRef]

35. He, H.; Xia, Q.; Wang, B.; Wang, L.; Hu, Q.; Zhou, A. Two-dimensional vanadium carbide (V$_2$CT) MXene as supercapacitor electrode in seawater electrolyte. *Chin. Chem. Lett.* **2020**, *31*, 984–987. [CrossRef]

36. Chen, Y.; Yao, H.; Kong, F.; Tian, H.; Meng, G.; Wang, S.; Mao, X.; Cui, X.; Hou, X.; Shi, J. V$_2$C MXene synergistically coupling FeNi LDH nanosheets for boosting oxygen evolution reaction. *Appl. Catal. B Environ.* **2021**, *297*, 120474. [CrossRef]

37. Kresse, G.; Hafner, J. Ab initiomolecular-dynamics simulation of the liquid-metal–amorphous-semiconductor transition in germanium. *Phys. Rev. B* **1994**, *49*, 14251–14269. [CrossRef]

38. Kresse, G.; Furthmüller, J. Efficient iterative schemes forab initiototal-energy calculations using a plane-wave basis set. *Phys. Rev. B* **1996**, *54*, 11169–11186. [CrossRef] [PubMed]

39. Blood, P.D.; Swenson, R.D.; Voth, G.A. Factors Influencing Local Membrane Curvature Induction by N-BAR Domains as Revealed by Molecular Dynamics Simulations. *Biophys. J.* **2008**, *95*, 1866–1876. [CrossRef]

40. Bi, Y.; Cai, Z.; Zhou, D.; Tian, Y.; Zhang, Q.; Kuang, Y.; Li, Y.; Sun, X.; Duan, X. Understanding the incorporating effect of Co^{2+}/Co^{3+} in NiFe-layered double hydroxide for electrocatalytic oxygen evolution reaction. *J. Catal.* **2018**, *358*, 100–107. [CrossRef]

41. Huang, W.L.; Zhu, Q.; Ge, W.; Li, H. Oxygen-vacancy formation in LaMO3 (M=Ti, V, Cr, Mn, Fe, Co, Ni) calculated at both GGA and GGA+U levels. *Comput. Mater. Sci.* **2011**, *50*, 1800–1805. [CrossRef]

42. Xie, Y.; Naguib, M.; Mochalin, V.N.; Barsoum, M.W.; Gogotsi, Y.; Yu, X.; Nam, K.-W.; Yang, X.-Q.; Kolesnikov, A.I.; Kent, P.R.C. Role of Surface Structure on Li-Ion Energy Storage Capacity of Two-Dimensional Transition-Metal Carbides. *J. Am. Chem. Soc.* **2014**, *136*, 6385–6394. [CrossRef] [PubMed]

43. Liu, A.; Liang, X.; Ren, X.; Guan, W.; Gao, M.; Yang, Y.; Yang, Q.; Gao, L.; Li, Y.; Ma, T. Recent Progress in MXene-Based Materials: Potential High-Performance Electrocatalysts. *Adv. Funct. Mater.* **2020**, *30*, 2003437. [CrossRef]

44. Wu, M.; He, Y.; Wang, L.; Xia, Q.; Zhou, A. Synthesis and electrochemical properties of V_2C MXene by etching in opened/closed environments. *J. Adv. Ceram.* **2020**, *9*, 749–758. [CrossRef]

45. Yu, M.; Wang, Z.; Liu, J.; Sun, F.; Yang, P.; Qiu, J. A hierarchically porous and hydrophilic 3D nickel–iron/MXene electrode for accelerating oxygen and hydrogen evolution at high current densities. *Nano Energy* **2019**, *63*, 103880. [CrossRef]

46. Wang, Z.; Wang, H.; Ji, S.; Wang, X.; Pollet, B.G.; Wang, R. Multidimensional regulation of $Ni_3S_2@Co(OH)_2$ catalyst with high performance for wind energy electrolytic water. *J. Power Sources* **2020**, *446*, 227348. [CrossRef]

47. Wang, Z.; Yu, K.; Feng, Y.; Qi, R.; Ren, J.; Zhu, Z.-Q. $VO_2(p)$-V_2C(MXene) Grid Structure as a Lithium Polysulfide Catalytic Host for High-Performance Li–S Battery. *ACS Appl. Mater. Interfaces* **2019**, *11*, 44282–44292. [CrossRef] [PubMed]

48. Yang, H.; Gong, L.; Wang, H.; Dong, C.; Wang, J.; Qi, K.; Liu, H.; Guo, X.; Xia, B.Y. Preparation of nickel-iron hydroxides by microorganism corrosion for efficient oxygen evolution. *Nat. Commun.* **2020**, *11*, 5075. [CrossRef] [PubMed]

49. Hu, L.; Li, M.; Wei, X.; Wang, H.; Wu, Y.; Wen, J.; Gu, W.; Zhu, C. Modulating interfacial electronic structure of CoNi LDH nanosheets with Ti_3C_2T MXene for enhancing water oxidation catalysis. *Chem. Eng. J.* **2020**, *398*, 125605. [CrossRef]

50. Li, X.; Hao, X.; Wang, Z.; Abudula, A.; Guan, G. In-situ intercalation of NiFe LDH materials: An efficient approach to improve electrocatalytic activity and stability for water splitting. *J. Power Sources* **2017**, *347*, 193–200. [CrossRef]

51. Liu, J.; Wang, J.; Zhang, B.; Ruan, Y.; Lv, L.; Ji, X.; Xu, K.; Miao, L.; Jiang, J. Hierarchical $NiCo_2S_4@NiFe$ LDH Heterostructures Supported on Nickel Foam for Enhanced Overall-Water-Splitting Activity. *ACS Appl. Mater. Interfaces* **2017**, *9*, 15364–15372. [CrossRef] [PubMed]

52. Liu, W.; Bao, J.; Guan, M.; Zhao, Y.; Lian, J.; Qiu, J.; Xu, L.; Huang, Y.; Qian, J.; Li, H. Nickel–cobalt-layered double hydroxide nanosheet arrays on Ni foam as a bifunctional electrocatalyst for overall water splitting. *Dalton Trans.* **2017**, *46*, 8372–8376. [CrossRef] [PubMed]

53. Zhao, Y.; Wan, W.; Chen, Y.; Erni, R.; Triana, C.A.; Li, J.; Mavrokefalos, C.K.; Zhou, Y.; Patzke, G.R. Understanding and Optimizing Ultra-Thin Coordination Polymer Derivatives with High Oxygen Evolution Performance. *Adv. Energy Mater.* **2020**, *10*, 2002228. [CrossRef]

54. Alkhalifah, M.A.; Howchen, B.; Staddon, J.; Celorrio, V.; Tiwari, D.; Fermin, D.J. Correlating Orbital Composition and Activity of $LaMn_xNi_{1−x}O_3$ Nanostructures toward Oxygen Electrocatalysis. *J. Am. Chem. Soc.* **2022**, *144*, 4439–4447. [CrossRef]

55. Sun, S.; Zhou, X.; Cong, B.; Hong, W.; Chen, G. Tailoring the d-Band Centers Endows $(Ni_xFe_{1−x})_2P$ Nanosheets with Efficient Oxygen Evolution Catalysis. *ACS Catal.* **2020**, *10*, 9086–9097. [CrossRef]

56. Song, Q.; Li, J.; Wang, S.; Liu, J.; Liu, X.; Pang, L.; Li, H.; Liu, H. Enhanced Electrocatalytic Performance through Body Enrichment of Co-Based Bimetallic Nanoparticles in Situ Embedded Porous N-Doped Carbon Spheres. *Small* **2019**, *15*, 1903395. [CrossRef] [PubMed]

57. Ma, W.; Ma, R.; Wu, J.; Sun, P.; Liu, X.; Zhou, K.; Sasaki, T. Development of efficient electrocatalysts via molecular hybridization of NiMn layered double hydroxide nanosheets and graphene. *Nanoscale* **2016**, *8*, 10425–10432. [CrossRef]

58. Wang, W.; Liu, Y.; Li, J.; Luo, J.; Fu, L.; Chen, S. NiFe LDH nanodots anchored on 3D macro/mesoporous carbon as a high-performance ORR/OER bifunctional electrocatalyst. *J. Mater. Chem. A* **2018**, *6*, 14299–14306. [CrossRef]

59. Jeong, S.; Hu, K.; Ohto, T.; Nagata, Y.; Masuda, H.; Fujita, J.-i.; Ito, Y. Effect of graphene encapsulation of NiMo alloys on oxygen evolution reaction. *ACS Catal.* **2019**, *10*, 792–799. [CrossRef]

60. Wang, Y.; Xie, C.; Zhang, Z.; Liu, D.; Chen, R.; Wang, S. In Situ Exfoliated, N-Doped, and Edge-Rich Ultrathin Layered Double Hydroxides Nanosheets for Oxygen Evolution Reaction. *Adv. Funct. Mater.* **2018**, *28*, 1703363. [CrossRef]

61. Teng, Y.; Wang, X.D.; Liao, J.F.; Li, W.G.; Chen, H.Y.; Dong, Y.J.; Kuang, D.B. Atomically thin defect-rich Fe-Mn-O hybrid nanosheets as high efficient electrocatalyst for water oxidation. *Adv. Funct. Mater.* **2018**, *28*, 1802463. [CrossRef]

62. Fang, H.; Huang, T.; Liang, D.; Qiu, M.; Sun, Y.; Yao, S.; Yu, J.; Dinesh, M.M.; Guo, Z.; Xia, Y. Prussian blue analog-derived 2D ultrathin $CoFe_2O_4$ nanosheets as high-activity electrocatalysts for the oxygen evolution reaction in alkaline and neutral media. *J. Mater. Chem. A* **2019**, *7*, 7328–7332. [CrossRef]

63. Du, C.F.; Sun, X.; Yu, H.; Fang, W.; Jing, Y.; Wang, Y.; Li, S.; Liu, X.; Yan, Q. $V_4C_3T_x$ MXene: A promising active substrate for reactive surface modification and the enhanced electrocatalytic oxygen evolution activity. *InfoMat* **2020**, *2*, 950–959. [CrossRef]

64. Wen, Y.; Wei, Z.; Liu, J.; Li, R.; Wang, P.; Zhou, B.; Zhang, X.; Li, J.; Li, Z. Synergistic cerium doping and MXene coupling in layered double hydroxides as efficient electrocatalysts for oxygen evolution. *J. Energy Chem.* **2021**, *52*, 412–420. [CrossRef]

65. Lu, Y.; Fan, D.; Chen, Z.; Xiao, W.; Cao, C.; Yang, X. Anchoring Co_3O_4 nanoparticles on MXene for efficient electrocatalytic oxygen evolution. *Sci. Bull.* **2020**, *65*, 460–466. [CrossRef]

66. Liu, Q.; Zhou, F.; Bai, Y.; Hu, W. Evaluating Properties of Carbon-Free Nano-NiCoFe-LDHs with Molybdate as Oxygen Evolution Catalysts and Their Applications in Rechargeable Air Electrodes. *Energy Fuels* **2021**, *35*, 20374–20385. [CrossRef]

67. Chen, J.; Long, Q.; Xiao, K.; Ouyang, T.; Li, N.; Ye, S.; Liu, Z.-Q. Vertically-interlaced NiFeP/MXene electrocatalyst with tunable electronic structure for high-efficiency oxygen evolution reaction. *Sci. Bull.* **2021**, *66*, 1063–1072. [CrossRef]

68. Chen, S.; Yu, C.; Cao, Z.; Huang, X.; Wang, S.; Zhong, H. Trimetallic NiFeCr-LDH/MoS_2 composites as novel electrocatalyst for OER. *Int. J. Hydrogen Energ.* **2021**, *46*, 7037–7046. [CrossRef]

69. Hao, C.; Wu, Y.; An, Y.; Cui, B.; Lin, J.; Li, X.; Wang, D.; Jiang, M.; Cheng, Z.; Hu, S. Interface-coupling of CoFe-LDH on MXene as high-performance oxygen evolution catalyst. *Mater. Today Energy* **2019**, *12*, 453–462. [CrossRef]

70. Ye, C.; Zhang, L.; Yue, L.; Deng, B.; Cao, Y.; Liu, Q.; Luo, Y.; Lu, S.; Zheng, B.; Sun, X. A NiCo LDH nanosheet array on graphite felt: An efficient 3D electrocatalyst for the oxygen evolution reaction in alkaline media. *Inorg. Chem. Front.* **2021**, *8*, 3162–3166. [CrossRef]

71. Han, S.; Chen, Y.; Hao, Y.; Xie, Y.; Xie, D.; Chen, Y.; Xiong, Y.; He, Z.; Hu, F.; Li, L.; et al. Multi-dimensional hierarchical CoS_2@MXene as trifunctional electrocatalysts for zinc-air batteries and overall water splitting. *Sci. China Mater.* **2020**, *64*, 1127–1138. [CrossRef]

72. Wang, J.; He, P.; Shen, Y.; Dai, L.; Li, Z.; Wu, Y.; An, C. FeNi nanoparticles on $Mo_2TiC_2T_x$ MXene@nickel foam as robust electrocatalysts for overall water splitting. *Nano Res.* **2021**, *14*, 3474–3481. [CrossRef]

73. Dai, W.; Ren, K.; Zhu, Y.-a.; Pan, Y.; Yu, J.; Lu, T. Flower-like $CoNi_2S_4$/Ni_3S_2 nanosheet clusters on nickel foam as bifunctional electrocatalyst for overall water splitting. *J. Alloys Compd.* **2020**, *844*, 156252. [CrossRef]

74. Gultom, N.S.; Abdullah, H.; Hsu, C.-N.; Kuo, D.-H. Activating nickel iron layer double hydroxide for alkaline hydrogen evolution reaction and overall water splitting by electrodepositing nickel hydroxide. *Chem. Eng. J.* **2021**, *419*, 129608. [CrossRef]

75. Babar, P.; Lokhande, A.; Karade, V.; Pawar, B.; Gang, M.G.; Pawar, S.; Kim, J.H. Bifunctional 2D Electrocatalysts of Transition Metal Hydroxide Nanosheet Arrays for Water Splitting and Urea Electrolysis. *ACS Sustain. Chem. Eng.* **2019**, *7*, 10035–10043. [CrossRef]

76. Yang, H.; Chen, Z.; Guo, P.; Fei, B.; Wu, R. B-doping-induced amorphization of LDH for large-current-density hydrogen evolution reaction. *Appl. Catal. B-Environ.* **2020**, *261*, 118240. [CrossRef]